

# Dimensionality Control of Li Transport by MOFs Based Quasi-Solid to Solid Electrolyte (Q-SSEs) for Li–Metal Batteries

M. Salado,<sup>\*[a, b, c]</sup> R. Fernández de Luis,<sup>[a]</sup> T. H. Smith,<sup>[b]</sup> M. Hasapoor,<sup>[b]</sup> S. Lanceros-Mendez,<sup>[a, c]</sup> and M. Forsyth<sup>[b, c]</sup>

Nowadays, lithium-ion batteries (LIBs) are widely used in all walks of life and play a very important role. As complex systems composed of multiple materials with diverse chemical compositions, where different electrochemical reactions take place, battery interfaces are essential for determining the operation, performance, durability and safety of the battery. This work, set out to study the incorporation of lithium bis(fluorosulfonyl)amide (LiFSI) doped 1-ethyl-3-methylimidazolium bis(trifluoromethylsulfonyl)imide ([EMIm][TFSI]) ionic liquid into an archetype Ti-based Metal Organic Framework (MOF) ((Ti) MIL125–NH<sub>2</sub>) to create a solid to quasi-solid (depending on the amount of IL in the system), and how it affects not only

ionic transport but also the structural properties of the IL/MOF electrolyte. Remarkably high ionic conductivity values ( $2.13 \times 10^{-3} \text{ S} \cdot \text{cm}^{-1}$  at room temperature) as well as a lithium transference number ( $t_{\text{Li}} = 0.58$ ) were achieved, supported by pulsed field gradient (PFG) NMR experiments. Electrochemical characterization revealed reversible plating-stripping of lithium and lower overpotential after 750 h at 50 °C. Additionally, a proof-of-concept solid state battery was fabricated resulting in a discharge capacity of 160 mAh·g<sup>-1</sup> at 50 °C and 0.1 C rate after 50 cycles. This work presents a suitable strategy to dendrite suppression capability, allowing its implementation as interface modifiers in next-generation solid-state batteries.

## Introduction

Since 1991, lithium-ion batteries (LIBs) have revolutionized modern society, finding application from portable electronics to electric vehicles, thanks to their impressive attributes, including high capacities (~372 mAh·g<sup>-1</sup>), high discharge voltages and exceptional Coulombic efficiencies. Most commercial LIBs use a metal oxide cathode, organic electrolyte and graphite as the anode due to the favourable combination of electrochemical performance and cost-effectiveness. However, as the world's energy demands continue to surge, traditional LIBs are gradually approaching their theoretical performance limits.<sup>[1,2]</sup>

In recent years, lithium metal batteries (LMBs) have taken a central role due to their remarkable theoretical specific capacity (~3860 mAh·g<sup>-1</sup>) and the lowest electrode potential (~3.04 V

vs. standard hydrogen electrode). While LMBs hold great promise in meeting up-scaling energy requirements, they grapple with intrinsic challenges.<sup>[3]</sup> In both cases, the nucleation of lithium and the formation of a solid electrolyte interphase (SEI) depend on various factors within the bulk electrolyte and at the electrode surface.<sup>[4]</sup> These factors play a pivotal role in dictating the subsequent processes of lithium deposition and dissolution. When lithium nucleation and SEI formation occur unevenly, the deposition and dissolution of lithium becomes erratic and uncontrollable.<sup>[5]</sup> This disparity leads to numerous unwanted issues, including the growth of lithium dendrites, the fracture of the SEI, unregulated volume expansion, the accumulation of "dead lithium", electrode corrosion and electrolyte depletion.<sup>[6–8]</sup> These complications collectively contribute to the failure of LMBs. Currently, generating a stable anode SEI involves an extended formation cycling process (~1 week), which entails substantial manufacturing costs.<sup>[3,9]</sup> Furthermore, the resistance associated with Li-ion transport through the SEI imposes limitations on the charging rate of LIBs. Hence, the development of the next generation of anode materials (e.g. Li–metal, silicon or modified-graphite) depends on the advancement of superior passivation layers and novel design of electrode surfaces.<sup>[10,11]</sup> These innovations are imperative for stabilizing high-capacity anode materials and paving the way for efficient and reliable energy storage solutions.

The exact composition of the SEI remains uncertain, but it is widely acknowledged to be a complex assembly of microphases (e.g. the mosaic model). This intricate structure typically consists of two distinct layers: an inner compact layer primarily composed of inorganic components and an outer porous layer rich in organic materials. The specific constituents of these

[a] Dr. M. Salado, Dr. R. Fernández de Luis, Prof. S. Lanceros-Mendez  
BCMaterials, Basque Center for Materials, Applications and Nanostructures  
UPV/EHU Science Park, 48940 Leioa, Spain  
E-mail: manuel.salado@bcmaterials.net

[b] Dr. M. Salado, Dr. T. H. Smith, Dr. M. Hasapoor, Prof. M. Forsyth  
Institute for Frontier Materials, Deakin University  
Burwood, VIC, 3125, Australia

[c] Dr. M. Salado, Prof. S. Lanceros-Mendez, Prof. M. Forsyth  
IKERBASQUE, Basque Foundation for Science  
48009 Bilbao, Spain

 Supporting information for this article is available on the WWW under  
<https://doi.org/10.1002/batt.202400134>

 © 2024 The Authors. *Batteries & Supercaps* published by Wiley-VCH GmbH. This is an open access article under the terms of the Creative Commons Attribution Non-Commercial NoDerivs License, which permits use and distribution in any medium, provided the original work is properly cited, the use is non-commercial and no modifications or adaptations are made.

layers depend on the extent of reduced phases resulting from the decomposition of the solvent.<sup>[4,7,12]</sup> To gain greater control over the chemical composition and morphology of the SEI, recent efforts have focused on incorporating multi-dimensional porous architectures into electrodes.<sup>[13–15]</sup>

These architectures offer significant benefits, including increased surface area, enhanced Li-ion diffusion, and ample internal space. These characteristics collectively inhibit the formation of lithium dendrites and provide sufficient capacity for lithium storage. Furthermore, the deliberate development of an artificial SEI represents a promising avenue for tailoring and optimizing the ideal chemistry and properties of this multi-layer interphase. In this regard, MOFs emerge as highly appealing candidates.<sup>[16]</sup> Through innovative synthetic design, MOFs can be engineered to possess specific attributes such as porosity, stability, lithiophilicity, particle morphology and conductivity.<sup>[17]</sup> These tailored MOFs enable precise control over the spatial confinement of  $\text{Li}^+$  ion flux, increasing the local  $\text{Li}^+$  ion concentrations and facilitating dendrite-free lithium deposition.<sup>[18]</sup> For example, Xiong et al.<sup>[19]</sup> demonstrated the advantages of an inorganic LiF-rich SEI in achieving exceptional electrochemical performance. Then, the introduction of F-moieties into MOF structures can actively participate in SEI formation, enriching the LiF phase, and suppressing SEI reconstruction. The remarkable versatility of MOFs in materials engineering addresses challenges such as sluggish ion diffusion and volumetric changes.

In addition, encapsulation of ionic liquids (ILs) into porous materials, in particular, MOFs, is a powerful strategy to achieve advanced properties by combining the advantages of both components.<sup>[20]</sup> Considering the richness and diversity of MOFs and ILs, a great variety of IL-incorporated MOF composites could be obtained. Most of the existing IL-MOFs have not been investigated as solid-state electrolytes (SSEs) for cation conduction. Moreover, different kinds of metal salts, together with various ILs, could be incorporated into the system. The loading of non-flammable and non-volatile ILs enables a good interfacial wettability with high safety for high-temperature batteries.<sup>[21]</sup> Generally, IL-MOFs are introduced into a polymeric matrix to enhance mechanical stability.<sup>[22]</sup> The ionic conductivities ( $10^{-5}$  to  $10^{-3} \text{ S}\cdot\text{cm}^{-1}$ ) of IL-MOF are mainly determined by the loading amount of IL, the types of MOFs, and the inner interactions. The current transference numbers of cations (0.3–0.4) are affected by the pore structure and surface property of MOFs.<sup>[23]</sup>

In the present work, (Ti) MIL-125–NH<sub>2</sub> was impregnated with a high concentrated (LiFSI) salt into the IL 1-ethyl-3-methylimidazolium bis (trifluoromethyl sulfonyl) amide [EMIm-TFSI]. This electrolyte with synergistic effect of TFSI and FSI anions, which not only effectively suppresses lithium dendrite growth because of the highly concentrated solid electrolyte interphase film, but also the presence of two anions, beneficially improve the cycling performance of lithium batteries.<sup>[24]</sup> The structural and physico-chemical characteristics of MIL125–NH<sub>2</sub> have been reported in myriad of studies reported before. First, from a structural point of view, the crystal structures of these MOFs are built up from twelve connected

titanium oxo-clusters connected through amino-terephthalic organic linkers. This connectivity gives rise to a tetragonally distorted framework with an “fcu” topology with two different pores of 6 and 12.5 Å diameters (Figure 1a). After the incorporation of the IL into MIL125–NH<sub>2</sub> extract the electrochemical properties as solid-state-electrolyte and finally, we tested as a proof-of-concept into a LMB.

## Results and Discussion

### Physicochemical Characterization

The main role of MIL125–NH<sub>2</sub> is to provide mechanical stability as well as the creation of a well oriented percolating medium where the flow of the IL component is favored for ion conduction. Thus, just in terms of size the IL components could be located in both positions of the structure. In the specific case of the small site with 6 Å of diameter, it is likely that only one of the IL components could be hosted at this position of the framework. When considering the pore with  $\varnothing=12.5$  Å, both components of the IL can be located at the same space within the scaffold of the MIL125–NH<sub>2</sub>. Depending on the MOF:IL weight ratio, the material turns from solid to quasi-solid as it can be observed a color change in the sample as well as the appearance, becoming a wetted solid (Figure 1b). The morphology of the sample MIL125\_IL (1:2) is presented was characterized by scanning electron microscopy (SEM) in Figure 1c. It is observed that a compact structure is formed from agglomerated MOF-particles covered by a thin layer of IL. This morphology suggests a possible double ionic transport mechanism, through the MOF pores as well as through the IL boundaries. The chemical interaction between the IL and the MOF was evaluated by Fourier Transform Infrared Spectroscopy (FTIR). The main difference in the 4000–2000  $\text{cm}^{-1}$  wavelength range after the inclusion of the IL into the porous structure is the disappearance of the O–H stretching vibration related to the presence of H<sub>2</sub>O (Figure S1, Supporting Info.). In the 2000–600  $\text{cm}^{-1}$  range the higher the amount of IL, leads to more pronounced absorbance bands related with the IL molecules, as expected. In particular two strong stress bands were observed related to the presence of TFSI and FSI groups, the first one at 610  $\text{cm}^{-1}$ , corresponding to the S=O bending, and the second one corresponding to the C–F stretching at 1190  $\text{cm}^{-1}$ . Also, a signal at 1129  $\text{cm}^{-1}$  is observed, ascribed to the S=O strain-symmetric bonding, while another band is also observed at 1331  $\text{cm}^{-1}$ , corresponding to an asymmetric C=O vibration.<sup>[25]</sup> Regarding the characteristic IR band fingerprints of MIL125–NH<sub>2</sub>, 1565 and 1412  $\text{cm}^{-1}$  are assigned to the C=C vibration of the aromatic ring in the organic ligand, meanwhile the stretching at 700  $\text{cm}^{-1}$  is ascribed to Ti–O–Ti stretching.<sup>[26]</sup> The absence of peak shift of all signals suggests the weak interaction between the MOF framework and the IL molecules after their blending into a composite electrolyte system. X-ray diffraction analysis of the as-synthesized MIL125–NH<sub>2</sub> and different MOF:IL ratios were performed in order to evaluate the impact of the IL inclusion on the MOF structure (Figure 2a).

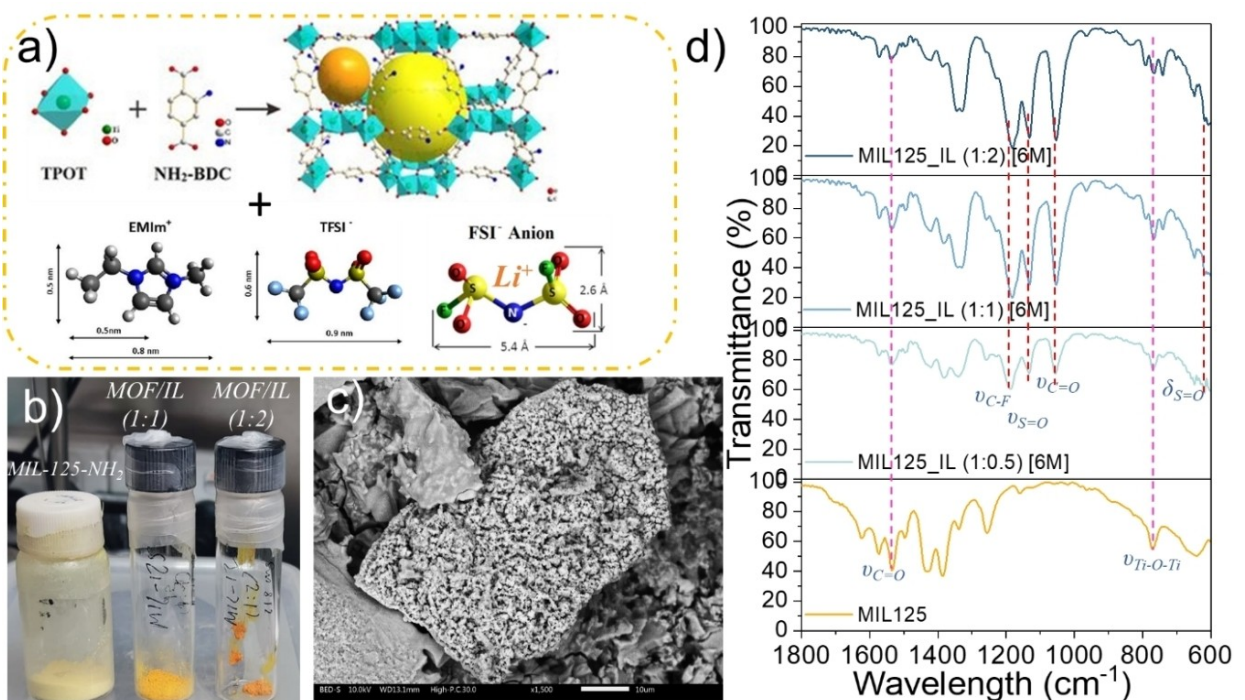


**Figure 1.** a) Chemical structure and size of the (Ti)  $\text{MIL125-NH}_2$  and the cation and anions that forms the IL (adapted from ref [27] and [28]). b) Physical appearance of the MOF as-synthesized and after mixing with 1:1 and 1:2 MIL125\_IL ratio. c) SEM image of the  $\text{MIL125\_IL (1:2)}$  sample and d) FTIR spectra of (Ti)  $\text{MIL125-NH}_2$  and after adding different amounts of IL (1:0.5, 1:1, 1:2). IR bands corresponding to (Ti)  $\text{MIL125-NH}_2$  are marked by pink dashed lines, and the bands corresponding to IL are marked by red dashed lines.

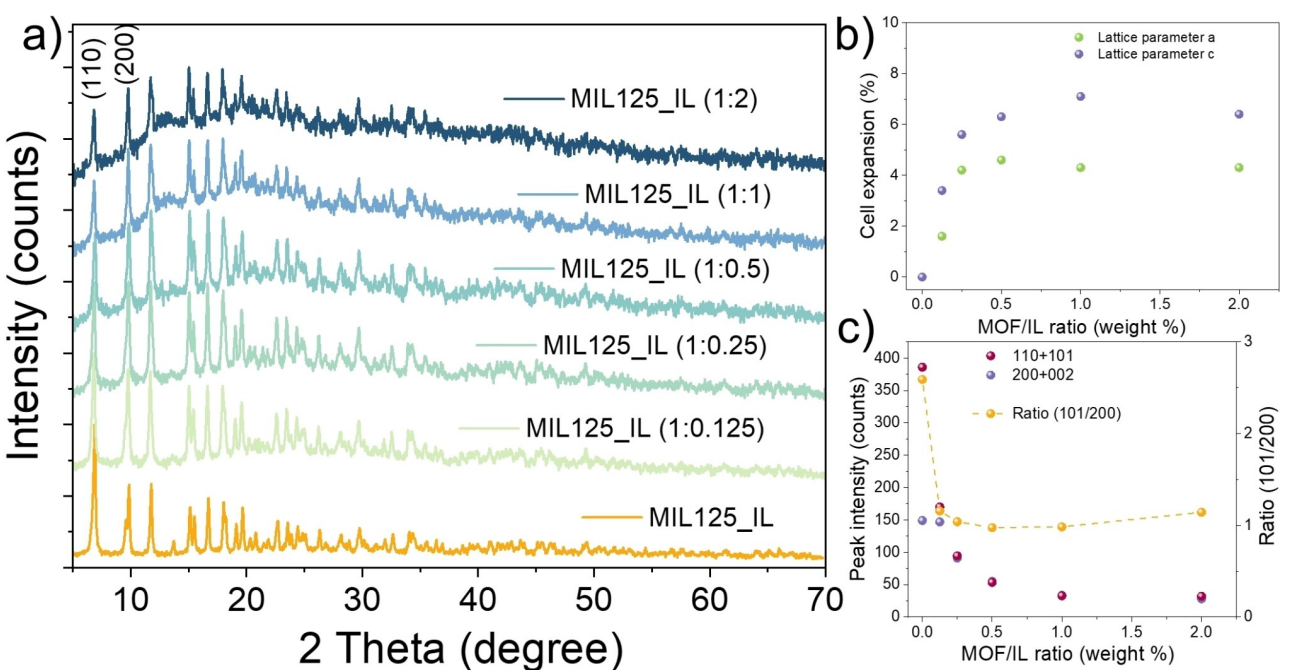


**Figure 2.** a) XRD patterns of  $\text{MIL125-NH}_2$  with different amounts of IL. b) Cell parameter evolution with different amounts of IL. c) First ( $110 + 101$ ) and the second ( $200 + 002$ ) reflexion ratio with different amounts of IL.

Generally, there is a drop in the intensity of the diffraction maxima, when IL is included in the MOF. In addition, an increase of the background incoherent scattering is observed indicating above a 1:0.5 MOF:IL weight ratio. This finding

suggests that once surpassed this threshold, the MOF is saturated and the IL starts to be stabilized as an interphase at the surface of the MOF particles.

Continuing with the XRD-data analysis, the evolution of the cell parameters when IL is added into the system was obtained after fitting the data with a full profile analysis without structural model, as depicted in the Figure 2b. According to literature, the  $I\bar{4}/mmm$  space group and the  $a=b=18.65\text{ \AA}$ ;  $c=18.131\text{ \AA}$ ;  $\alpha=\beta=\gamma=90^\circ$  cell parameters were employed as the starting point of the fitting. In general terms, there is a slight expansion of the cell volume ( $\sim 1\%$ ) when the IL is included into MIL125-NH<sub>2</sub> up to a MOF:IL weight ratio of 1:0.5. Above this IL loading, the diffraction patterns do not change. It is suggested that once the MOF:IL – 1:0.5 loading is surpassed, not all the IL enters into the MOF structure, as it was observed in the SEM image. To firmly confirm this hypothesis, the change in relative intensity in the reflections was calculated. For that, the ratio between the intensity of the first maximum (110 + 101) and the second (200 + 002), is showed in Figure 2c. The variation of the relative intensities in the XRD-data confirms that once incorporated into the pore space the IL molecules follows in some degree the long-range order of the MIL125-NH<sub>2</sub> framework. That is to say that the IL-solvent included within the MOF is not fully disordered. Both the parameters and the relative intensity only vary up to a MOF:IL ratio of 1:0.5 by weight. Therefore, MOF is already saturated at this IL-loading, being the excess of IL encased it in a thin shell at the surface of the MOF-particles., in agreement with SEM image (Figure 1c).

High-pressure CO<sub>2</sub> adsorption isotherms of MOF and MOF:IL (1:0.5) samples were measured at 0 °C in order to estimate the surface area of both materials (Figure S2). The isotherms for both compounds show a type-I profile, where most of the CO<sub>2</sub> uptake occurs in the low-pressure region. This is characteristic of microporous materials.<sup>[29]</sup> When comparing the parent MOF with the IL loaded one, there is a significant decrease of the CO<sub>2</sub> uptake, specially at lower pressures. That is, the micro porosity of the framework is partially blocked. Even though XRD data suggest that the structure is fully saturated by IL, the CO<sub>2</sub> isotherms, and BET data (1088 m<sup>2</sup>·g<sup>-1</sup> for MIL125-NH<sub>2</sub> and 195.30 m<sup>2</sup>·g<sup>-1</sup> for MOF:IL (1:0.5) suggest that the pore blocking by IL molecules is not fully effective. The small mismatch between the geometry and volume of the pores in MIL125-NH<sub>2</sub>, and the molecular volume of the IL components, can promote the presence of a residual porosity with the framework of the MOF:IL. Still, the overall porosity reduction confirms that the IL is integrate within the pore space of the MIL125-NH<sub>2</sub>.

The UV Raman spectra of MIL125-NH<sub>2</sub> were analyzed with varying amounts of ionic liquid to probe their interaction with the framework structure (Figure S3). Prominent bands at 803, 1254, 1414, and 1611 cm<sup>-1</sup> were observed under an 830 nm excitation. The resonance-enhanced Raman band at 803 cm<sup>-1</sup> is ascribed to titanium species within octahedral coordination environments, where each titanium atom is linked to six oxygen atoms. Furthermore, bands at 546, 1234, and 1414 cm<sup>-1</sup> are attributed to the bending and symmetric stretching of framework Ti–O–Ti–O ring species. Although, spectra shown in the figures were normalized to the highest peak, EMImTFSI fluorescence overlap MOF signal on the whole range, making impossible extract any useful information.

## Electrochemical Characterization

The ionic conductivity of a solid electrolyte gives not only information of the electrochemical performance but also of its temperature stability. Although the optimal operating temperature range for LIBs when carbonate electrolytes is limited to 15–35 °C, the use of MIL125-IL solid electrolytes allow an operation temperature range above 100 °C with no significant degradation as both materials are stable at high temperatures.<sup>[30,31]</sup>

Consequently, the temperature dependence of the ionic conductivity for the different MIL125-IL samples was characterized by EIS, from room temperature up to 80 °C (Figure S4). In addition, samples with an IL with lower molarity (e.g. 3 M) with weight ratio 1:1 and 1:2 were prepared to compare whether a low viscosity could help to improve the ionic conductivity. All samples showed high ionic conductivities, being MIL125-IL (1:2) samples the most promising with ionic conductivities in the range of 10<sup>-3</sup> S·cm<sup>-1</sup> compared to a lower ratio (10<sup>-4</sup> S·cm<sup>-1</sup>). Regarding the influence in the viscosity of the IL, no significant effect has been observed. It is suggested as the system is saturated of IL, ions can be transport through the pores or through the particles boundaries. To assess the influence of adding IL on the movement of ions within the MOF channels and in the boundaries, analyzing the activation energies associated with ionic conductivity can serve as a valuable indicator of possible underlying mechanism. These activation energies are determined using the Arrhenius equation:

$$\sigma = A \cdot e\left(\frac{-E_a}{RT}\right)$$

where  $\sigma$  is the conductivity obtained from the EIS measurements (S·cm<sup>-1</sup>),  $A$  is the Arrhenius constant,  $E_a$  is the activation energy (J·mol<sup>-1</sup>),  $R$  is the gas constant (8.31 J·K<sup>-1</sup>·mol<sup>-1</sup>) and  $T$  is the absolute temperature (K).

Activation energy was calculated for all samples by the Arrhenius equation (Figure 3a), obtaining a value of 15.05 kJ·mol<sup>-1</sup> and 22.15 kJ·mol<sup>-1</sup> for MIL125-IL (1:2) and MIL125-IL (1:1), respectively. It was previously demonstrated (ref) that a lower activation energy could offer alleviated polarization, stabilizing the electrolyte-electrode interfaces. Consequently, it is expected that MIL125-IL (1:2) samples due to an excess of IL, could create a better interface contact with the electrode and improve the battery performance.

To investigate the diffusivity of the Li<sup>+</sup> ions, pulsed field gradient (PFG) NMR diffusion measurements were employed to acquire deeper insights into the relative mobility of cations in MIL125-IL system depending on the ratio and to better comprehend the transport properties at a molecular level. As expected, the diffusion coefficient of lithium ions exhibits a monotonous increase as a function of temperature from 20 to 80 °C.

The resulting <sup>7</sup>Li diffusion coefficients for MIL125-IL (1:2) and (1:1) samples are given in Figure 3b. For both samples, the diffusion coefficients increase with temperature. However, the

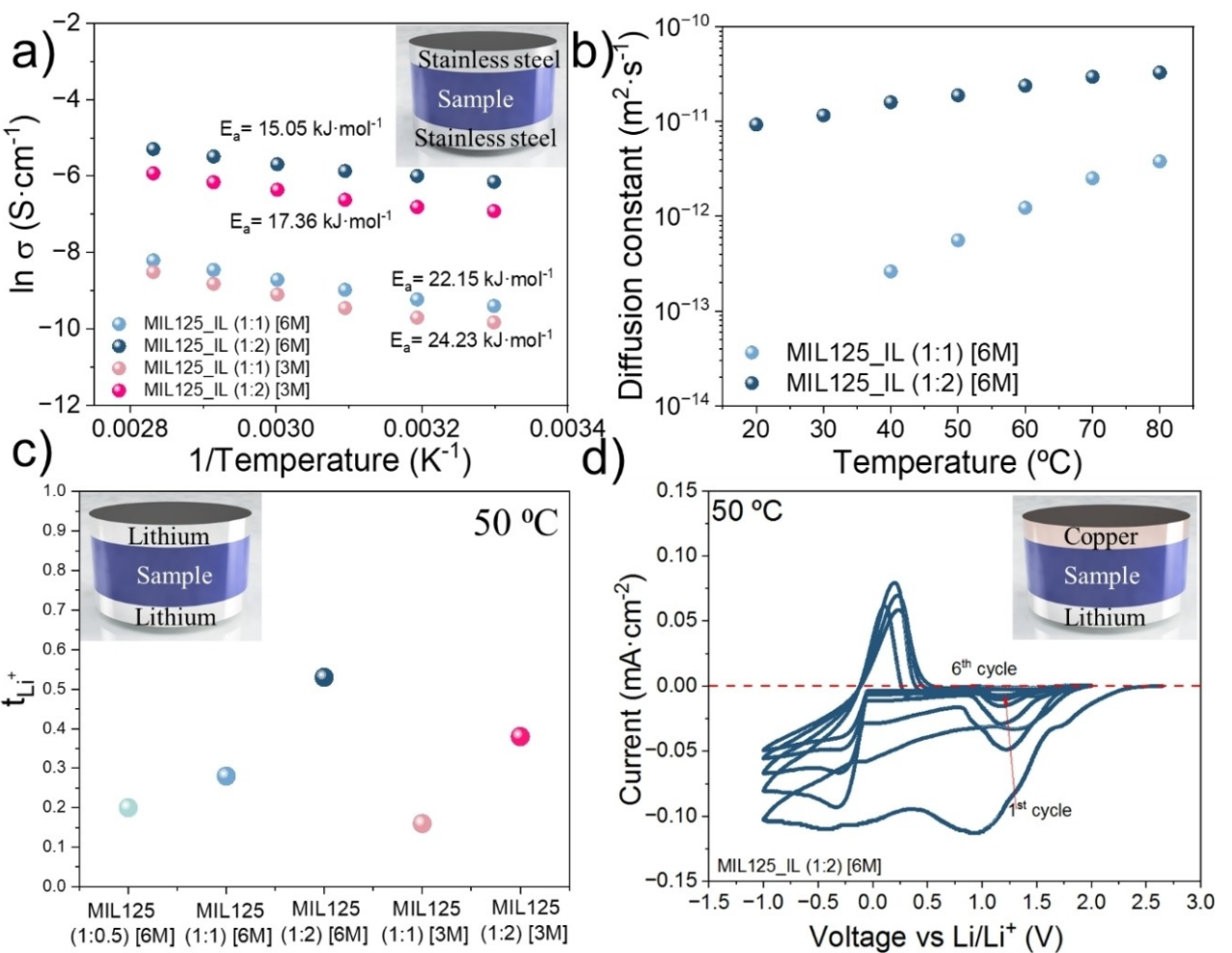


**Figure 3.** a) Arrhenius plot of the conductivity vs. the inverse of the temperature for extracting the activation energy of each MOF:IL ratio. b) Evolution of lithium diffusion constant with temperature extracted from pulsed field gradient (PFG) NMR diffusion measurements. c) Lithium transference number for different MOF:IL ratios and different molarity. d) Cyclic voltammetry of the lithium plating-stripping reaction at the cooper interface of the MIL125\_IL (1:2) sample.

diffusion coefficients for the MIL125\_IL (1:2) sample are significantly higher than that of the MIL125\_IL (1:2) sample. This indicates that there is greater Li<sup>+</sup> mobility in the (1:2) sample, this correlates with the previous results. It is important to stress the importance of the amount of IL in the sample to assist the Li<sup>+</sup> mobility. For instance, the sample MIL125\_IL (1:1) is high temperature dependent as it showed lithium ion diffusion from 40 °C compare with the 1:2 ratio.

Despite numerous efforts to enhance electrochemical performance, current MOF-based electrolyte materials still struggle to strike a balance among ionic conductivity, Li<sup>+</sup> transference number, and operating temperature range.<sup>[17,32–34]</sup> Although an electrolyte may exhibit outstanding ionic conductivity, it is the transference number that dictates the quantity of beneficial cations capable of being transported between the electrodes in a rechargeable metal-ion battery.

As it was expected, samples with higher amount of IL results in higher Li<sup>+</sup> transference number extracted by the Bruce-Vincent method (Figure S5). For instance, MIL125\_IL (1:2) gives an encouraging value of 0.58, displaying the effectiveness of

the combination of MOF and IL as solid or quasi-solid electrolyte.

According to previous studies, the porous structure of MOFs, enhance the transport of Li<sup>+</sup> ions compare to liquid electrolytes which have an average value lower than 0.5.<sup>[35]</sup> Regarding the samples with lower molarity, they followed the same trend as their concentrated counterpart but with a lower value.

Once the good electrochemical properties of the combination of MOFs and ILs had been proved, it was also important to check the electrochemical stability for use in a battery. For that, the effect of the additives on the electrochemical stability window (ESW) of the electrolytes was determined via linear sweep voltammetry (LSV), using the complex electrolyte system MIL125\_IL (1:2) [6 M]. LSV was carried out using a stainless-steel working electrode and a lithium counter and reference electrodes. As it can be observed in Figure S6, the sample presents electrochemical stability toward an anodic oxidation condition. In particular, an electrochemical stability up to 4 V was obtained for the solid electrolyte at 50 °C. Consequently, there is

negligible electrolyte degradation when LFP is used as cathode material.

Researchers are currently exploring various approaches to stabilize the plating and stripping behavior through electrolyte modification, current collector engineering, interphase engineering, or the development of advanced cycling protocols. In order to evaluate the reversible lithium plating-stripping reaction, a MIL125\_IL (1:2) sample was placed between Cu|Li electrodes with a sweep rate was  $0.1 \text{ mV}\cdot\text{s}^{-1}$ .

As Figure 3d shows, when the 1<sup>st</sup> anodic scan started, one peak was observed between 0.5 V and +1.5 V. Nevertheless, the intensity of this signal diminished significantly in the 2<sup>nd</sup> to 6<sup>th</sup> cycles. This peak at a potential of 1.4 V vs Li | Li<sup>+</sup> can be attributed to the breakdown of TFSI anions. This reaction is catalyzed by Li<sup>+</sup> cations, facilitated by induced changes within the double layer.<sup>[36]</sup> The decomposition of the TFSI anion as well as the presence of the FSI anion, resulted in the creation of a stable SEI layer, a critical component for ensuring a prolonged cycle life in Li-ion and Li-metal based batteries. It is suggested that during the first cycle, there is a SEI formation process on Cu (first cycle) and then during Li plating in the consecutive cycles.<sup>[37]</sup> Average Li CE was extracted from a Li|Cu half cell (Figure S7). To minimize the effect of the roughness and the possible surface oxide from Cu substrate, Li was deposited to create a Li reservoir. After 48 cycles the calculated CE value was 85.24%.

To unequivocally demonstrate the reversible nature of metal plating/stripping, galvanostatic cycling tests were performed for the three MIL125\_IL ratios (e.g. 1:0.5, 1:1 and 1:2). A lower overpotential would suggest an ease of deposition/stripping from the lithium foil surface, and therefore its compatibility with metal batteries. As it can be seen in Figure 4a, the three samples showed overpotentials lower than 0.2 V under the galvanostatic cycling tests of Li|Li symmetric cells with current densities of  $0.5 \text{ mA}\cdot\text{cm}^{-2}$ , being a good performance for a solid electrolyte. However, different behaviors shown by the symmetric cells could tentatively be explained by an improved interfacial contact. After cycling samples MIL125\_IL (1:0.5) and MIL125\_IL (1:1), results in a rising overpotentials after 85 h and 215 h, respectively and a consequent short-circuit of the cell. This suggests the formation of a thick interfacial layer, which ultimately compromises subsequent cycling performance. This behaviour can be attributed to a non-uniform electrolyte/lithium interface. On the other hand, MIL125\_IL (1:2) samples, presented a uniform and stable behaviour, up to 750 h. This good stability agrees with previous studies that prove a highly concentrated IL electrolytes provides stable performance in both Li-symmetrical and Li-full cells. Moreover, they exhibit inherent non-flammability, mitigating safety concerns associated with Li-metal reactivity when used with carbonate-based electrolytes, and remain thermally stable even at elevated temperatures. To assess cyclic performance and ensure compatibility with lithium metal batteries (LMBs), cells were assembled with a Li-metal anode and LiFePO<sub>4</sub> (LFP) as the cathode material. LFP, favoured for its eco-friendliness, affordability and moderate capacity, imposes limitations on cathode-related degradation due to the low potential cut-off

(2.5 V) typically employed in LFP cells.<sup>[38]</sup> Unlike other cathode material chemistries, LFP cathodes do not contain expensive metals, such as cobalt and nickel, that was main reason to select LFP as cathode material. Also, the thermal stability of LFP cathodes makes the suitable to use our solid-state electrolyte. Based on the ESW data (Figure S6), LFP is the optimal candidate due to its operational cut-off voltage aligning with the stable range of the electrolyte. From the perspective of electrolyte combinations, MIL125\_IL (1:2) exhibits superior performance thanks to its higher ionic conductivity, better diffusion constant, and higher Li transference number, as illustrated in Figure 3. Nevertheless, further improvements should be done to have a better insight of the compatibility with this electrolyte.

The cyclability of Li|LFP cells containing MIL125\_IL ratios (1:1 and 1:2) were assessed at C/10 at 50 °C over 55 cycles. The evolution of charge-discharge capacity and Coulombic efficiencies is illustrated in Figure 4b, with the reported values derived from the best-performing cells among three for each electrolyte. The corresponding voltage profiles are depicted in Figure S8a and b. The variation in the coulombic efficiency in the beginning cycles Figure 4b (top), can be ascribed to the formation of the SEI. It has been already proved as not 100% of the lithium ions released from the positive electrode during charging return to the positive electrode during discharge. As it has been aforementioned, the formation of a stable SEI is crucial for an efficient battery. Comparing the evolution of the charge-discharge capacity, it can be observed as the MIL125\_IL (1:1) sample suffers from a loss of capacity after cycling meanwhile the MIL125\_IL (1:2) sample, displayed a remarkable discharge capacity of  $160 \text{ mAh}\cdot\text{g}^{-1}$  at 50 °C and 0.1 C rate after 55 cycles. This trend correlates with Li-transference numbers, as well as the high ionic conductivity calculated. It is envisaged then that the synergistic effect of the high ionic conductivity and nanowetted interface between the MOF and the electrode would entail a high-capacity and good dendrite suppression capability, allowing its implementation in next-generation solid-state batteries. MIL125\_IL ratio (1:2) electrolyte was chosen to be cycled at different C-rates as it has shown good performance in Li|LFP cells. As depicted in Figure 4c and S9, the cell cycled stably up to a charge rate of C/2. Even faster cycling was achieved on charging at 1 C, however there was a drop in the capacity retention and this was even lower at 2 C. This drop in discharge capacity at high C-rate could be ascribed to the high thickness of the MIL125\_IL (1:2) sample, as electrode thickness, porosity and tortuosity are the major parameters that affect the rate performance. When cycling returned to C/10, the initial capacity is restored. This behaviour suggests that the solid electrolyte is not degraded after high cycling and/or lithium dendrites have been formed. Nevertheless, further studies of transport kinetics should be done to understand this process.

A better insight of the cell behavior after cycling, can be obtained by a post-mortem analysis to validate the solid-state electrolyte. For that, the morphology (SEM and XRD) and the element distribution after cycling has been performed. According to Figure S10, it seems that the crystal structure form the MOF does not change during the cycling measurement, but the unit cell might shrink a bit while the crystallite size decreases

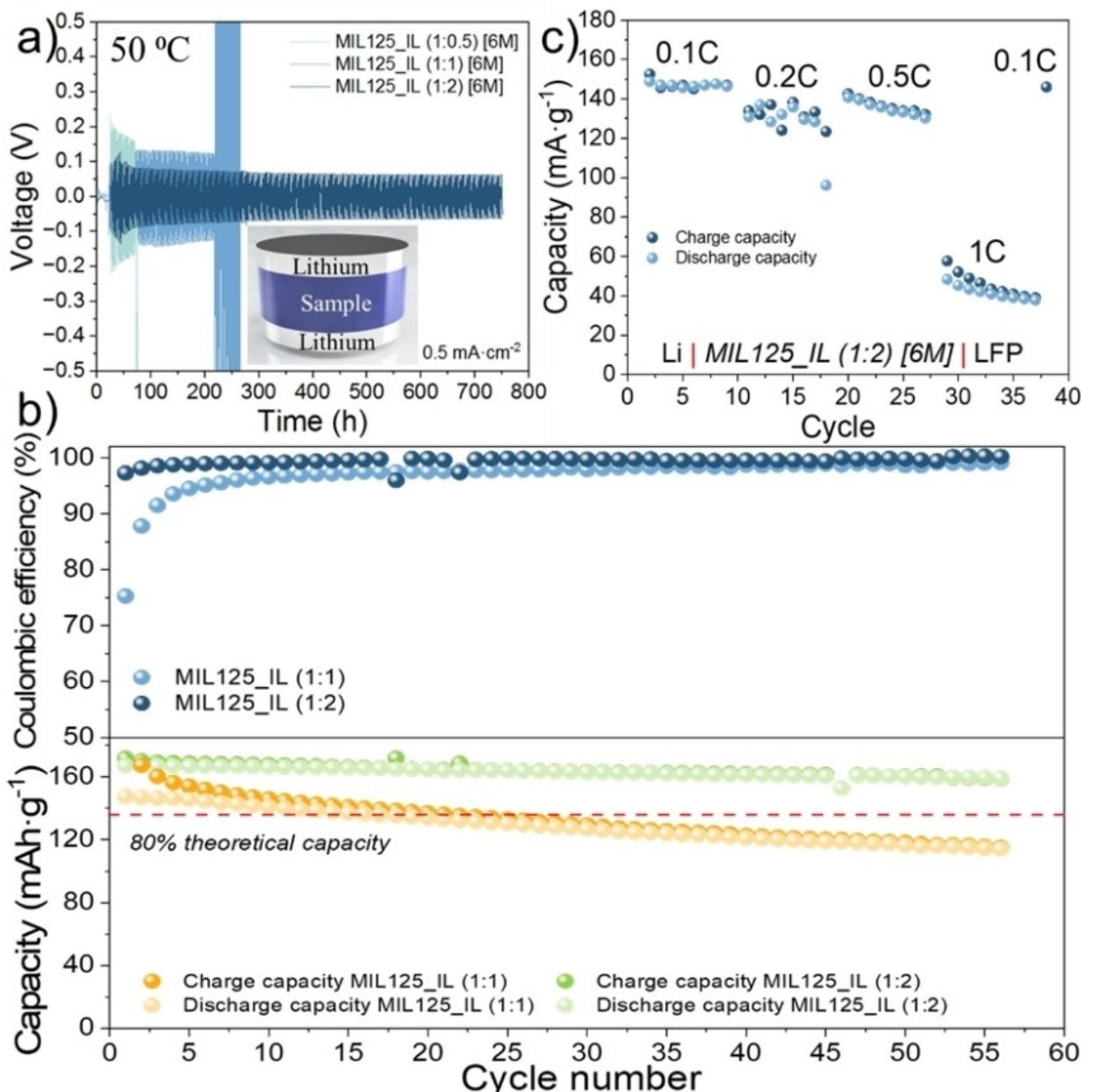


**Figure 4.** a) Galvanostatic cycling test of Li|Li symmetric cells with different MOF:IL ratios (1:0.5, 1:1 and 1:2) at the current density of 0.5 mA·cm<sup>-2</sup>. b) Coulombic efficiency and capacity retention during galvanostatic cycling at C/10 of Li|LFP at 50 °C with MIL125\_IL (1:1) and MIL125\_IL (1:2), respectively. c) Rate capability performance of MIL125\_IL (1:2) in Li|LFP at 50 °C.

with observable peak broadening. **Figure S11** depicts the cross-sectional and top-view of a dissembled cell after rate capability test. The thickness of the solid-electrolyte consists of 560 µm, the softness of the solid electrolyte guarantees continuous and efficient Li<sup>+</sup> pathways in the solid electrolyte. However, it did not allow the electrolyte/lithium interface to be observed properly, due to the complexity of the sample preparation. SEM analysis were performed on lithium metal surface from a cell after 80 cycles. **Figure S12**, represents lithium anode after removing partially the solid electrolyte MIL125\_IL (1:2) [6 M]. It can be observed the absence of dendrites, as it was expected from the good performance of this composition. Moreover,

Energy-dispersive X-ray spectroscopy (EDX) was carried out to understand the possible SEI formation. Taking two different areas of the SEM image, we could identify the possible composition. Spectrum 6, which correspond to lithium metal surface, only three elements were identified, C, F and O. Consequently, we suggest the formation of an inorganic rich layer, possibly formed by LiF, Li<sub>2</sub>O, Li<sub>2</sub>CO<sub>3</sub>. On the other hand, spectrum 7 extracted from the solid electrolyte area, it can be identified Ti, characteristic from the MOF structure. This fact can be attributed to a proper passivation layer being formed. Interestingly, a thinner layer can be used as an interface modifier towards safer, high-performance and high-energy-

density lithium batteries. When element analysis is performed (**Figure S13**) on the cross-section image, Ti as well as S, the characteristic elements of (Ti) MIL125–NH<sub>2</sub> and TFSI and FSI, are well distributed along the electrolyte. Nevertheless, it was observed a high concentration of O<sub>2</sub> in the interface electrolyte/lithium that is in accordance with the top-surface from lithium metal. During discharge, oxygen undergoes a sequential reduction process, initially forming superoxide radical anions and subsequently evolving into LiO<sub>2</sub> and Li<sub>2</sub>O<sub>2</sub>. Unfortunately, numerous aprotic electrolytes are not resilient in the presence of these two products, leading to an undesirable consequence of reducing the cycle life of the batteries. It has been proposed that the high stability together with the excellent adhesion between Li metal and the MIL125\_IL (1:2) electrolyte, is crucial for facilitating efficient ion transfer and ensuring long cycle life. As Li anodes are prone to receding a few microns during discharge if the solid electrolyte (e.g. MIL125\_IL (1:1)) lacks good adhesion to the Li. Consequently, the resulting void can escalate interfacial resistance and diminish overall ionic conductivity.

## Conclusions

In this work, the excellent properties of MOF and ILs have been combined to fabricate electrolytes from solid to quasi solid state, depending on the amount IL added into the system, with potential applications as a solid electrolytes in lithium batteries. It has been demonstrated that ILs have been successfully incorporated into the MOF structure, however it has been demonstrated the importance of a wetted interface first, to improve lithium ion transport through the solid electrolyte and secondly to create a better adhesion when Li metal is used as anode. Among the different samples, MIL125\_IL (1:1) resulted in high ionic conductivities, high lithium transference number, high diffusion constant and low activation energy. The latest entails a lower polarization at the interface that correlates with low deposition/stripping overpotentials. Low overpotentials are also indicative of low interfacial resistance between the electrodes and the electrolyte. As proof-of-concept, a Li|MIL125\_IL|LFP full battery was assembled which resulted in excellent performance with a capacity discharge of 160 mAh·g<sup>-1</sup> after 55 cycles. Also, post-mortem analysis concluded in an absence of lithium dendrite formation even if the cell has been measured at 2 C rate. This work paves the way to the synthesis of new chemistry of solid-to quasi-solid-state electrolytes for lithium batteries.

## Materials and Methods

### Materials

N,N-Dimethylformamide (DMF) (99.9%), ethanol (98%) and methanol (99.9%) were obtained from LABKEM. 2-Aminoterephthalic acid (BDC–NH<sub>2</sub>, 98%), Ti(IV) isopropoxide solution were further supplied by Sigma Aldrich. All chemicals were used as provided.

### Synthesis of (Ti) MIL125–NH<sub>2</sub>

(Ti) MIL-125–NH<sub>2</sub> was prepared using established methods as reported previously.<sup>[39]</sup> In summary, 6 mmol of 2-amino benzene dicarboxylic acid (Sigma-Aldrich, 99%) was dissolved in 25 mL of N,N-dimethylformamide (DMF, Sigma-Aldrich, ≥99.8%) through stirring at room temperature for 5 minutes. Subsequently, 3 mmol of titanium isopropoxide (Sigma-Aldrich, ≥97%) was added dropwise until complete homogenization, followed by the addition of 25 mL of methanol (Sigma-Aldrich, 99.8%). The resulting mixture was stirred for an additional 30 minutes. The solution was then transferred to a 65 mL Teflon-lined stainless-steel autoclave and heated at 150 °C for 16 hours. The resulting solid was centrifuged (5000 rpm, 5 min) and subjected to three washes with DMF and three washes with methanol (100 mL each time for 30 minutes). The final yellow solid was recovered by centrifugation, dried at 60 °C overnight, and stored.

### High Salt Concentrated Ionic Liquid [EMIm][TFSI]

The [EMIm][TFSI] IL was saturated with the lithium salt (LiFSI). To ensure complete dissolution of the LiFSI in the IL, the solution was transferred to an ultrasonic bath for 5 min at room temperature. The final concentration of the obtained solution was 6 M. Finally, to remove any remaining moisture, it was left to dry in a Schlenk line at 100 °C for 72 h.

### Insertion of Li[FSI][EMIm][TFSI] into (Ti) MIL125–NH<sub>2</sub>

The Li-enriched IL was inserted by diffusion into the porous structure of the MOF after reactivating the MOF at 100 °C for at least 12 h. Five different MOF:IL weight ratios were prepared in order to study, first the insertion of the IL into the porous structure and secondly, the electrochemical properties. In a typical procedure, first an ethanolic solution of Li-[EMIm][TFSI] solution with a 10 mg·mL<sup>-1</sup> concentration was prepared. In a second step, 50 mg of MIL125–NH<sub>2</sub> was weighted in a glass-vial. Third, a given volume of the IL-solution was added to the MOF under stirring. The volume was chosen to finally obtain the desired MOF:IL weight ration once the ethanol was evaporated while stirring the mixture at moderate temperature (80 °C).

### Cell Fabrication

Li|Li symmetrical cells and Li metal and lithium iron phosphate (LiFePO<sub>4</sub> (LFP)) as electrodes were prepared using CR2032 (Hohsen) coin cell components. The cathode (LFP) was vacuum-dried at 100 °C for 48 h and other cell components were vacuum-dried for 24 h at 50 °C and were kept in an argon-filled glovebox. A soft-bristled toothbrush was used to brush the oxide film off the Li foil (50 µm thickness was used directly without any passivation) (Gelon LIB Co., Ltd.), and 10 mm diameter Li disks were punched using a steel punch. LFP (CustomCells) with an active mass of 1.4 mAh·g<sup>-1</sup> was cut into 8 mm diameter disks (0.5 cm<sup>-2</sup>) and used as the cathode.

### Characterization

#### Physicochemical Characterization

The Fourier Transform Infrared Spectra (FTIR) of various materials were acquired by analyzing the samples within the range of 4000–600 cm<sup>-1</sup> at room temperature using a JASCO FT/IR-6100 spectrophotometer equipped with Attenuated Total Reflectance (ATR) at a

resolution of  $4\text{ cm}^{-1}$ . 64 scans were measured and averaged to obtain the final spectra.

X-ray diffraction patterns of the parent MOF and the MOF:IL composites were acquired formed at room temperature using a Panalytical X-pert Cu  $\text{K}\alpha_{1,2}$  diffractometer in the  $2\theta$  range from 5 to  $70^\circ$  with a  $0.02^\circ$  step. The data was fitted with a full-profile matching analysis without structural model. The final fittings allow to extract the integrated intensity of the diffraction maxima located at low  $2\theta$  ( $^\circ$ ) interval. The ratio of the integrated intensities of the (110) and (101) versus the (200) + (002) planes was followed when integrating the IL into the pore space of MIL-125-NH<sub>2</sub>. Refinement was conducted based on the R-3 spatial group utilizing the cell parameters derived from the single-crystal data through the FULLPROF SUITE program. Employing the Pattern Matching technique, the evolution of the cell parameters after adding the IL into the structure was calculated.

Both parent MIL-125-NH<sub>2</sub>, and MOF:IL (1:0.5) samples were activated during four hours at  $125^\circ\text{C}$  under vacuum. The activation temperature was limited in order to prevent any damage of the MOF by the IL in the MOF:IL composite. CO<sub>2</sub> sorption isotherms (0.01–30 bars) were measured at  $0^\circ\text{C}$  on a Quantachrome instruments ISorb HP1 pressure gas sorption analyser, with the surface area values obtained by fitting to a linearized form of the Brunauer Emmet Teller (BET) equation of the adsorption data. Kinetic data for each adsorption point was measured until equilibrium. The adsorption data was treated as explained by C.J. Kim et al.<sup>[40]</sup> in order to obtain the BET surface area.

Raman measurements were carried out in backscattering geometry by exciting the samples at 830 nm with a wavelength (Raman Renishaw inVia Qontor). Measurements were performed at room with a Laser power between 0.1 and 2 mW and A 50x microscopic objective focuses light on the sample and collects the generated Raman light signal to a dichroic mirror.

To study the top-view and cross-section morphology and to determine the element distribution of the cross-section and the solid electrolyte/lithium interface formed after cycling of the MIL125\_IL (1:2) sample, SEM (scanning electron microscopy) and EDX (energy dispersive X-ray spectroscopy) were used. The coin cells were disassembled inside an argon-filled glovebox using a coin cell disassembly unit (Hohsen). Then a JEOL JSM-IT300 Oxford was used with a 10 kV acceleration voltage.

### Electrochemical Characterization

To evaluate the electrochemical performance of the different IL:MOF weight ratios, 5 mm diameter samples were compact to obtain a thickness of 200  $\mu\text{m}$ . The ionic conductivity was assessed by electrochemical impedance spectroscopy (EIS) on a EL-CELL connected to a Biologic SP-300 potentiostat. The frequency range measured was from 1 Hz to 1 MHz, employing a signal amplitude of 10 mV. The electrochemical behavior of the material was examined across a temperature range from room temperature to  $80^\circ\text{C}$ . Prior to the impedance measurement, the samples were equilibrated at each temperature for 30 minutes. To extract the main parameter, the Nyquist plot were fitted using the Zview 3.0 software. The ionic conductivity was determined using Equation:

$$\sigma = \frac{t}{A \cdot R}$$

where  $t$  is the thickness,  $A$  is the area of the sample and  $R$  correspond to the resistance extracted from the Nyquist plot.

Pulsed field gradient (PFG) NMR experiments were performed on a 7.05 T Bruker Avance III MHz wide-bore solid-state NMR spectrometer, equipped with a 5 mm Diff50 probe. Samples were packed into 4 mm solid-state NMR rotors in an Ar glovebox, which were subsequently placed inside 5 mm NMR glass tubes for the experiments. Before each measurement, the temperature was allowed to equilibrate for at least 10 minutes. The PFG stimulated echo (STE) pulse sequence was used. Gradient pulse lengths and diffusion times were varied depending on the sample and temperature, but typical values used were 2 ms and 20 ms respectively and the maximum gradient strength used was  $2900\text{ G}\cdot\text{cm}^{-1}$ . The signal attenuation profiles were fitted in TopSpin software to obtain diffusion coefficients.

The Li<sup>+</sup> transference number was determined by the Bruce-Vincent method using a Li symmetric cell. For that, a CR2032 (Hohsen) coin cell was assembled using a symmetric configuration within an Ar-filled glove box, using Li foil as electrodes. Then, a polarization test was carried out at  $50^\circ\text{C}$  using Biologic SP-300 potentiostat with a perturbation voltage amplitude of 10 mV. Before and after the experiment, Impedance spectra measured in the frequency range from 1 Hz to 1 MHz were recorded. Accordingly, the Li<sup>+</sup> transference number can be extracted using the following equation:

$$t_{\text{Li}^+} = \frac{i_\infty(\Delta V - i_0 R_0)}{i_0(\Delta V - i_\infty R_\infty)}$$

where  $i_0$  is the initial current,  $i_\infty$  is the current in the steady state,  $R_0$  and  $R_\infty$  are the resistances before and after applying the polarization, respectively, and  $\Delta V$  is the applied potential.

The Li<sup>+</sup>/Li redox behavior in different electrolytes was investigated using either a stainless-steel electrode (Figure 3a) or a copper electrode (Figure 3d) as the counter and working electrode (WE), and lithium metal as the reference electrode (RE) using a CR2032 (Hohsen) coin cell. Linear Sweep voltammetry (LSV) analysis was conducted using a Biologic SP-300 potentiostat within an oven at  $50^\circ\text{C}$ . A scan rate of  $0.1\text{ mV}\cdot\text{s}^{-1}$  was employed for investigating lithium plating and stripping behavior.

Cu electrode was used as the working electrode and the Li electrode was used as the counter and reference electrode. To minimize the effect of Cu substrate, in this new experiment, we use a different method. The average CE over 48 cycles was calculated by the following equation:

$$CE_{\text{Avg}} = \frac{nQ_c + Q_s}{nQ_c + Q_t}$$

Where  $Q_t$  is the reservoir capacity deposited onto the Cu substrate,  $(Q_c)$  is charge used to cycle Li between working and counter electrodes for  $n$  cycles. And  $Q_s$ , is the final stripping charge corresponding to the quantity of Li remaining after cycling, is measured. To determine the Li CE in MIL125\_IL (1:2) [6 M], the reservoir capacity  $Q_t$  of  $3.5\text{ mAh}\cdot\text{cm}^{-2}$  was deposited at  $0.35\text{ mA}\cdot\text{cm}^{-2}$ , then Li was cycled with a capacity  $Q_c$  of  $0.4\text{ mAh}\cdot\text{cm}^{-2}$  at  $0.35\text{ mA}\cdot\text{cm}^{-2}$  for 48 cycles. Finally, the remaining Li was stripped at  $0.35\text{ mA}\cdot\text{cm}^{-2}$  to 1 V and the charge  $Q_s$  was measured.

To perform the long-term stability cycling, the Li-metal full cells underwent a 24-hour rest period at  $50^\circ\text{C}$  before undergoing cycling at C/10 (21  $\mu\text{A}$ ) for 100 cycles at  $50^\circ\text{C}$ . For rate capability tests, Li-metal full cells were charged to 4 V and discharged to 2.5 V at various rates between C/10 and 1 C followed by additional cycles at C/10, at  $50^\circ\text{C}$  on a Neware battery cycler.

## Supporting Information

Supporting information is available.

## Acknowledgements

M.S acknowledges the funding from the European Union H2020 Program under the Marie Curie global fellowship (ROCHE, 101026163). T.H.S acknowledges the Australian Research Council (ARC) Centre for Training Centre for Future Energy Storage Technologies (storEnergy) (IC180100049). Open Access publishing facilitated by Deakin University, as part of the Wiley - Deakin University agreement via the Council of Australian University Librarians.

## Conflict of Interests

The authors declare no conflict of interest.

## Data Availability Statement

The data that support the findings of this study are available in the supplementary material of this article.

**Keywords:** Metal Organic Framework • Ionic liquid • dendrite-free • energy storage • solid-state electrolyte

- [1] J. B. Goodenough, K.-S. Park, *J. Am. Chem. Soc.* **2013**, *135*, 1167–1176.
- [2] C. P. Grey, D. S. Hall, *Nat. Commun.* **2020**, *11*, 2–5.
- [3] M. Tomasov, M. Kajanova, P. Bracinik, D. Motyka, *Transp. Res. Procedia* **2019**, *40*, 548–555.
- [4] Z. Ahmad, V. Venturi, H. Hafiz, V. Viswanathan, *J. Phys. Chem. C* **2021**, *125*, 11301–11309.
- [5] W. W. Wang, Y. Gu, H. Yan, K. X. Li, Z. Bin Chen, Q. H. Wu, C. Kranz, J. W. Yan, B. W. Mao, *Faraday Discuss.* **2021**, *233*, 190–205.
- [6] S. E. Sandoval, M. T. McDowell, *Matter* **2023**, *6*, 2101–2102.
- [7] B. Li, Y. Chao, M. Li, Y. Xiao, R. Li, K. Yang, X. Cui, G. Xu, L. Li, C. Yang, Y. Yu, D. P. Wilkinson, J. Zhang, *A Review of Solid Electrolyte Interphase (SEI) and Dendrite Formation in Lithium Batteries*, Springer Nature Singapore, 2023.
- [8] H. Adenusi, G. A. Chass, S. Passerini, K. V. Tian, G. Chen, *Adv. Energy Mater.* **2023**, *13*, DOI 10.1002/aenm.202203307.
- [9] F. Dai, M. Cai, *Commun. Mater.* **2022**, *3*, DOI 10.1038/s43246-022-00286-8.
- [10] M. R. Kumar, S. Singh, H. M. Fahmy, N. K. Jaiswal, S. Akin, A. E. Shalan, S. Lanceros-Mendez, M. Salado, *J. Power Sources* **2023**, *556*, 232256.
- [11] I. H. Buchberger, *Electrochemical and structural investigations on lithium-ion battery materials and related degradation processes*, Thesis from Technische Universität München (TUM), **2016**, 192
- [12] B. Jagger, M. Pasta, *Joule* **2023**, *7*, 1–17.
- [13] Y. K. Lee, K. Y. Cho, S. Lee, J. Choi, G. Lee, H. I. Joh, K. S. Eom, S. Lee, *Adv. Energy Mater.* **2023**, *13*, DOI 10.1002/aenm.202203770.
- [14] G. Lu, J. Nai, D. Luan, X. Tao, X. W. Lou, *Sci. Adv.* **2023**, *9*, 21–26.
- [15] A. M. Divakaran, M. Minakshi, P. A. Bahri, S. Paul, P. Kumari, A. M. Divakaran, K. N. Manjunatha, *Prog. Solid State Chem.* **2021**, *62*, 100298.
- [16] J. Andreo, R. Ettlinger, O. Zaremba, Q. Peña, U. Lächelt, R. F. De Luis, R. Freund, S. Canossa, E. Ploetz, W. Zhu, C. S. Diercks, H. Gröger, S. Wuttke, *J. Am. Chem. Soc.* **2022**, *144*, 7531–7550.
- [17] S. Bhattacharya, T. K. Maji, *Coord. Chem. Rev.* **2022**, *469*, 214645.
- [18] T. Wei, J. Lu, M. Wang, C. Sun, Q. Zhang, S. Wang, Y. Zhou, D. Chen, Y. Q. Lan, *Chin. J. Chem.* **2023**, *41*, 1861–1874.
- [19] Y. Li, W. Chen, T. Lei, H. Xie, A. Hu, F. Wang, J. Huang, X. Wang, Y. Hu, C. Yang, J. Xiong, *Energy Storage Mater.* **2023**, *59*, 102765.
- [20] X. Li, K. Chen, R. Guo, Z. Wei, *Chem. Rev.* **2023**, *123*, 10432–10467.
- [21] K. Liu, Z. Wang, L. Shi, S. Jungsuttiwong, S. Yuan, *J. Energy Chem.* **2021**, *59*, 320–333.
- [22] D. Han, Z. Zhao, W. Wang, H. Wang, H. Wang, L. Zheng, J. Shi, X. Li, *Sustain. Energy Fuels* **2022**, *6*, 4528–4538.
- [23] M. Urigoiti-Rodríguez, S. Vaquero-Vilchez, A. Mirandona-Olaeta, R. de Luis, E. Goikolea, C. M. Costa, S. Lanceros-Mendez, A. Fidalgo-Marijuan, I. de Larramendi, *Front. Chem.* **2022**, *10*, DOI 10.3389/fchem.2022.995063.
- [24] F. Chen, M. Forsyth, *J. Phys. Chem. Lett.* **2019**, *10*, 7414–7420.
- [25] J. Kiefer, J. Fries, A. Leipertz, *Appl. Spectrosc.* **2007**, *61*, 1306–1311.
- [26] S. Hu, M. Liu, K. Li, Y. Zuo, A. Zhang, C. Song, G. Zhang, X. Guo, *CrystEngComm* **2014**, *16*, 9645–9650.
- [27] R. Xue, H. Guo, W. Yang, S.-L. Huang, G.-Y. Yang, *Adv. Compos. Hybrid Mater.* **2022**, *5*, 1595–1611.
- [28] J. Marták, Š. Schlosser, *Front. Chem.* **2019**, *7*, DOI 10.3389/fchem.2019.00117.
- [29] E. Fernandez, P. G. Saiz, N. Peřinka, S. Wuttke, R. Fernández de Luis, *Adv. Funct. Mater.* **2021**, *31*, 2010703.
- [30] M. Z. Hussain, M. Bahri, W. R. Heinz, Q. Jia, O. Ersen, T. Kratky, R. A. Fischer, Y. Zhu, Y. Xia, *Microporous Mesoporous Mater.* **2021**, *316*, 110957.
- [31] Y. Cao, T. Mu, *Ind. Eng. Chem. Res.* **2014**, *53*, 8651–8664.
- [32] A. E. Abdelmaoula, J. Shu, Y. Cheng, L. Xu, G. Zhang, Y. Xia, M. Tahir, P. Wu, L. Mai, *Small Methods* **2021**, *5*, 1–9.
- [33] P. Mondal, S. M. Cohen, *Chem. Sci.* **2022**, *13*, 12127–12135.
- [34] F. Tao, L. Tian, Z. Liu, R. Cui, M. Liu, X. Kang, Z. Liu, *J. Mater. Chem. A* **2022**, *10*, 14020–14027.
- [35] Y. Yuan, K. Xue, Y. Ma, X. Peng, B. Wang, X. Liu, M. Liu, Y. Song, H. Lu, *Electrochim. Acta* **2023**, *440*, 141753.
- [36] M. Tułodziecki, J.-M. Tarascon, P.-L. Taberna, C. Guéry, *Electrochem. Commun.* **2017**, *77*, 128–132.
- [37] T. Shiga, Y. Masuoka, H. Nozaki, *RSC Adv.* **2021**, *11*, 13359–13365.
- [38] G. Ji, J. Wang, Z. Liang, K. Jia, J. Ma, Z. Zhuang, G. Zhou, H.-M. Cheng, *Nat. Commun.* **2023**, *14*, 584.
- [39] A. Gómez-Avilés, M. Peñas-Garzón, J. Bedia, D. D. Dionysiou, J. J. Rodríguez, C. Belver, *Appl. Catal. B* **2019**, *253*, 253–262.
- [40] K. C. Kim, T.-U. Yoon, Y.-S. Bae, *Microporous Mesoporous Mater.* **2016**, *224*, 294–301.

Manuscript received: February 29, 2024

Revised manuscript received: June 1, 2024

Accepted manuscript online: June 7, 2024

Version of record online: July 16, 2024